Atmospheric atomic mercury monitoring using differential absorption lidar techniques

Edner, H; Faris, G. W; Sunesson, A; Svanberg, Sune

Published in:
Applied Optics

DOI:
10.1364/AO.28.000921

1989

Atmospheric atomic mercury monitoring using differential absorption lidar techniques

Hans Edner, Gregory W. Faris, Anders Sunesson, and Sune Svanberg

Three-dimensional mapping of atmospheric atomic mercury has been performed with lidar techniques, to our knowledge, for the first time. Industrial pollution monitoring, as well as measurements of background concentrations, is reported. High-efficiency frequency doubling of narrowband pulsed dye laser radiation was employed to generate intense radiation at the mercury UV resonance line. Field measurements were supplemented with extensive laboratory investigations of absorption cross sections and interfering lines of molecular oxygen.

I. Introduction

Range-resolved monitoring of atmospheric atomic mercury pollution employing the differential absorption lidar technique is reported, we believe, for the first time. A mobile lidar system that was equipped with a narrowband tunable laser transmitter able to generate pulses of adequate power at the mercury resonance line at around 254 nm was employed. Interfering absorption lines due to molecular oxygen were studied in detail to allow mercury measurements with a sensitivity down to typical background levels, 2 ng/m^3.

Atomic mercury is an atmospheric pollutant that is directly generated from chlorine–alkali plants, coal-fired power plants and refuse–incineration plants. However, anthropogenic mercury enters the environment also in the aquatic phase as water-soluble mercury compounds, e.g., CH_3HgCl and $HgCl_2$. Again, industrial activities as well as inadequate waste management are responsible for such emissions. A complex and not fully understood interaction between the water and atmospheric phases occurs in the environmental mercury cycle.[1,2] Atomic mercury is also an interesting geophysical tracer gas associated with certain ore deposits,[3–6] as well as geothermal,[7,8] seismic,[9] and volcanic[10] activities.

Typical background concentrations of atomic mercury are a few ng/m^3.[11–13] Low concentrations of Hg are normally measured by point monitors employing gold amalgamation techniques combined with flameless atomic absorption spectroscopy.[14,15] Direct optical absorption or Zeeman absorption spectrometers can also be utilized.[16] Remote sensing techniques, such as lidar (light detection and ranging), and in particular the differential absorption lidar (DIAL)[17,18] provide important advantages over point monitoring. Typical Hg concentrations, which are exceedingly low by DIAL standards, can still be measured by that technique only since the oscillator strength of the electronic transition at 254 nm is concentrated in an atomic line rather than spread over the large number of rotational–vibrational molecular transitions normally encountered. Actually, mercury is the only pollutant that is present in the troposphere in elemental form. Because of the sharpness of the mercury absorption line a narrowband laser transmitter is necessary to attain maximum absorption when the laser is tuned to resonance with the line. For range-resolved lidar measurements that rely on atmospheric backscattering, a substantial laser pulse energy is necessary to achieve a useful range of ~1 km.

Early attempts to measure mercury with the DIAL technique are reported in Ref. 19. Sensitivity and range were severely limited by the large linewidth of the laser used (0.015 nm) and low output pulse energy (0.5 mJ) obtained by stimulated Raman scattering in H_2 of frequency-doubled dye laser radiation (567 nm). To exploit a broad laser, the gas correlation lidar technique[20] was introduced and demonstrated for Hg. By recording on- and off-resonance signals simultaneously, a greater immunity to atmospheric turbulence is obtained, but the sensitivity is reduced. In a parallel development we have also explored the potential of path-averaged measurements of mercury[21] with the DOAS (differential optical absorption spectroscopy) method.[22,23] Although this method is quite useful, it is very difficult to achieve high spectral resolution to

When this work was done all authors were with Lund Institute of Technology, Physics Department, P.O. Box 118, S-221 00 Lund, Sweden; G. W. Faris is now with SRI International, Molecular Physics Laboratory, Menlo Park, California 94025, and A. Sunesson is now with RIVM, Laboratory for Air Research, P.O. Box 1, 3720 BA Bilthoven, The Netherlands.

Received 17 March 1988.
0003-6935/89/050921-10$02.00/0.

obtain optimal sensitivity and freedom from the influence of interfering lines.

Three-dimensional, highly sensitive mapping of Hg, reported in this paper, had to await the availability of high-power narrowband pulsed laser sources at 254 nm. The measurements were performed with our new mobile lidar system[24] which, for this measurement, was equipped with a Quantel Datachrome system with a dual wavelength option and a linewidth of 0.001 nm in the UV. Using a betabarium borate (BBO) crystal, pulse energies up to 5 mJ could be generated by direct frequency doubling.

In the next section the mobile lidar system arrangements for the field work are described as well as the setup for laboratory measurements of the Hg cross section and interfering O_2 lines. Laboratory measurements are described in Sec. III.A while the field work is reported in Sec. III.B. Results for plumes from a chlorine–alkali plant are presented as well as measurements on background concentrations of Hg. In a separate section the lidar signal contributions due to Hg resonance fluorescence are discussed. Fluorescence is normally of little importance in tropospheric lidar work on molecules but is utilized in lidar monitoring of stratospheric atomic layers.[25,26] For Hg, in atomic form, fluorescence occurs even at tropospheric pressures and can contribute substantially to the signal when polarization techniques are employed. Finally, conclusions are drawn in the last section.

II. Experimental Arrangement

The system that was used has been described extensively in Ref. 24. It is housed in a mobile truck with a laboratory area of 6.0×2.3 m^2. Power is supplied by a 20-kVA diesel generator installed in a trailer towed by the truck.

A Nd:YAG-pumped dye laser is tuned alternately to two close-lying wavelengths, one that is on the mercury resonance line and one that is off the line. The laser beam passes a 6× beam expander and is transmitted into the atmosphere using quartz prisms and a large plane mirror housed in a dome construction that is hoisted up through a trapdoor in the roof of the truck during measurements. The large mirror can be rotated around both the horizontal and the vertical axes, thus allowing the beam to be aimed in the desired direction. Backscattered radiation is collected with the same mirror and directed into a Newtonian telescope with a 400-mm diameter. After the telescope, an interference filter selects the appropriate wavelength range for the detection. Detection is performed with an EMI 9816QA photomultiplier tube. The photomultiplier is gain-modulated to reduce the dynamic range of the signal and the mean power dissipation in the tube.

The electronic signal is A–D converted in one of the two channels of a LeCroy transient recorder with 10-ns time resolution. A GPIB interface transfers the digitized signal to an IBM AT-compatible computer where data are averaged and stored on floppy disks. During a measurement the system is controlled by the computer. It handles laser wavelength switching, measurement direction setting, and control of data sampling and data averaging. Up to three plume scans with fifteen directions each can be performed without interference from the operator. Both horizontal and vertical sweeps are possible.

For this measurement the system was equipped with a new Quantel YG 581C Nd:YAG laser and a TDL 50 dye laser. The pump laser delivers pulse energies of 500 and 200 mJ at 532 and 355 nm, respectively, with 10-Hz pulse repetition rate. The dye laser can deliver up to 200 mJ at 560 nm with a linewidth of 0.08 cm^{-1}. To generate the 254-nm radiation the dye laser was operated with coumarin 500 at 507 nm and the output was frequency doubled with a betabarium borate (BBO) crystal, supplied by CSK Co., Los Angeles. Betabarium borate is a relatively new material for nonlinear optical processes. It has a high damage threshold, good thermal stability, and it allows efficient doubling down to ~200 nm. It was possible to generate pulse energies of up to ~5 mJ at 254 nm from a dye laser pulse energy of 25 mJ at 507 nm. The linewidth of the frequency-doubled laser beam was 0.001 nm. To tune the dye laser on and off resonance a dual-wavelength feature supplied by Quantel was utilized. In the dye laser oscillator the rear end of the cavity is split into two parts. The two parallel beams are, after reflection from the single grating, tuned by two individual mirrors. The two cavities are tuned together by the laser wavelength tuning mechanism and the wavelength of the second cavity can be offset relative to that of the first one. A small chopper that blocks the two cavities alternately as it rotates is mounted in the intracavity space and a computer-controlled stepper motor rotates the chopper, thus alternately allowing the laser to oscillate on one of the two wavelengths. This is advantageous compared with moving the tuning mechanism of the laser at 5 Hz, which can cause undesirable vibrations and wavelength instability.

To calibrate the dye laser wavelength 10% of the outgoing beam is split off with a beam splitter and directed into a calibration unit. After passage through neutral-density filters it is split by a 50% beam splitter, and one part of it is passed through a thin quartz cell containing a drop of mercury in air while the other part is used as a reference beam. The intensities of the two beams are measured using photodiodes. The signals are A–D converted in the transient recorder, which is run as a boxcar averager by the computer. Measurements of the mercury differential absorption cross section were performed with the same unit.

The setup shown in Fig. 1 was used for the laboratory measurements, where the oxygen absorption spectrum around the mercury line was studied. The laser system and the data acquisition system in the mobile lidar system were used. The laser beam was directed from the truck, which is docked to the laboratory when it is not used in a field campaign, to an optical table where a mirror directed it through a lens and a diaphragm to the input window of a White multipass cell that was constructed in our laboratory.[27] The cell length is 2 m

and its body is a Pyrex tube with end flanges of stainless steel that, together with Invar rods, make up the frame of the device. The mirrors are Al and MgF_2 coated for maximum UV reflectance. Path lengths up to 200 m with lamps and 500 m with lasers have been achieved. A He–Ne laser was used to align the cell. After the cell, the beam passed through one more diaphragm and a lens and reached the detector, and EMI 9558 QA photomultiplier tube. The signal could be viewed directly on an oscilloscope, while to collect the data the transient recorder and the computer were utilized. To provide a marker of the mercury line position the part of the beam that was split off for calibration was passed through a thick mercury cell in the calibration unit and was detected by a photodiode. This signal was also digitized in the transient recorder and stored together with the spectra.

III. Measurements

A. Laboratory Measurements

Laboratory measurements were performed to establish the possible interference from oxygen absorption in a measurement of mercury vapor in the atmosphere. The setup illustrated in Fig. 1 was utilized, where the White multipass cell was filled with 1 atm of pure oxygen. The path length through the cell was adjusted by observing the signal from the PMT at the output, either directly on an oscilloscope or after digitization on the transient recorder. A read out from the latter is shown in Fig. 2. The sharp peak originates from the transmitted laser light, while the signal at shorter delay times/distances is due to scattered light in sequential reflections within the cell. The absorption was measured by integrating the channels containing the signal from the transmitted laser beam and normalizing to a few channels for the first reflections. This constituted an easy way of compensating for fluctuating laser power during a wavelength scan, without inserting a beam splitter and an additional photodetector. Thus, possible problems with fringes and different characteristics of two photodetectors were avoided. During an absorption measurement the noise was lowered by using a small capacitor on the PMT, which distributed the signal due to the transmitted light over more channels in the transient recorder. The path length used during the experiments was 340 m.

Figure 3(a) shows the measured oxygen absorption in a region close to the mercury resonance line. A recorded Hg spectrum is inserted as a dotted line. An enlargement of the Hg cell spectrum is shown in Fig. 3(b). The comparatively broad structure of the Hg line is due to the different isotopic and hyperfine structure lines present, as indicated in the figure.[28] The typical linewidth of these lines at atmospheric pressure, together with the laser linewidth used, is also inserted. As can be seen from Fig. 3(a) two weak oxygen lines are very close to the mercury line. These two lines lie on the long-wavelength side of the $v = 0 - v = 7$ band of the Herzberg I system but can neither be identified with Herzberg's listings nor with later listings of the Herzberg I, II, and III systems, to our knowledge.[29–33] The interference from these lines in a DIAL measurement of low background values of Hg over long atmospheric paths can be minimized if the two wavelengths are chosen carefully. With the laser linewidth of 0.001 nm used here, one wavelength can be placed on the Hg absorption peak, while the reference wavelength must avoid the oxygen lines. In the present measurement we used a wavelength difference of 0.008 nm with the reference on the long-wavelength side.

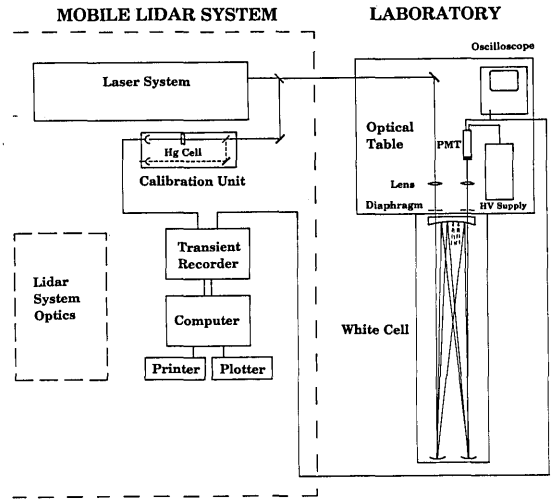

Fig. 1. Experimental arrangement.

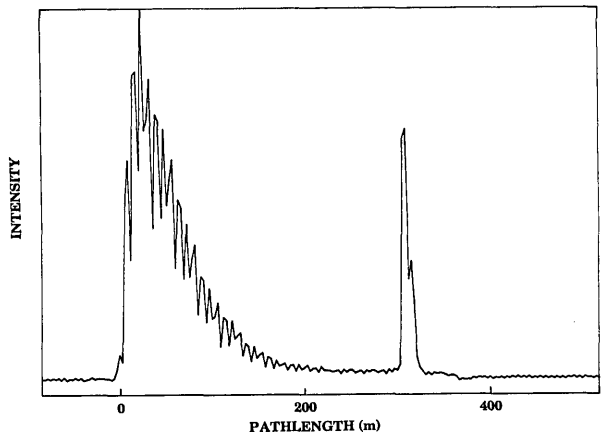

Fig. 2. Temporally resolved White cell signal.

The relevant Hg absorption cross section for the present system was established by measuring the absorption in several small Hg cells of known sizes and temperature. The results are plotted in Fig. 4, yielding a cross section of 3.3×10^{-18} m^2 or 9.8×10^{-6} m^2/ng.

B. Field Measurements

During a one-week period the mobile lidar system was used in a field measurement of Hg emission from a chlorine–alkali plant, which uses mercury in the process. The system was placed ~550 m from the largest Hg emission source, which was the outlet from a 60-m long clerestory 13 m above the ground. Measurements

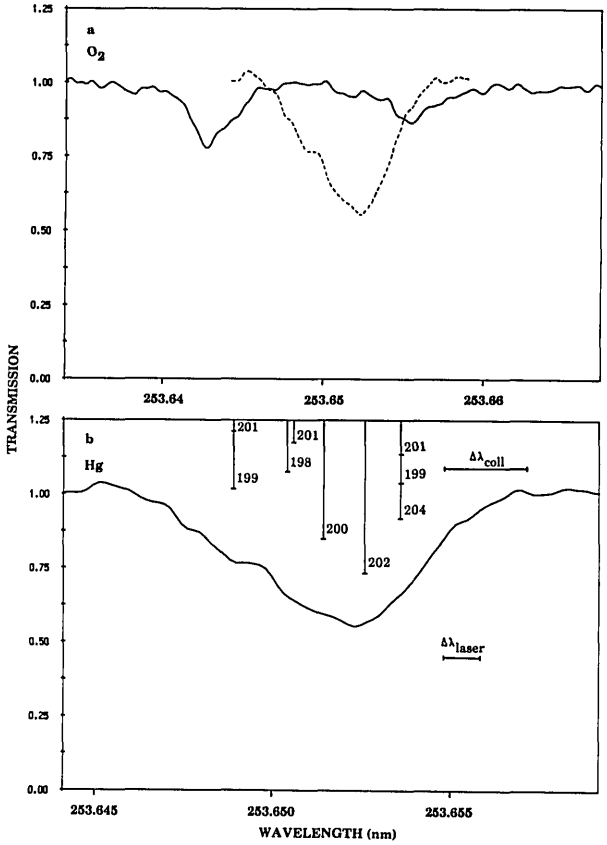

Fig. 3. Cell spectra: (a) overview with oxygen interference and (b) enlarged Hg signal with isotopic and hyperfine structure lines indicated.

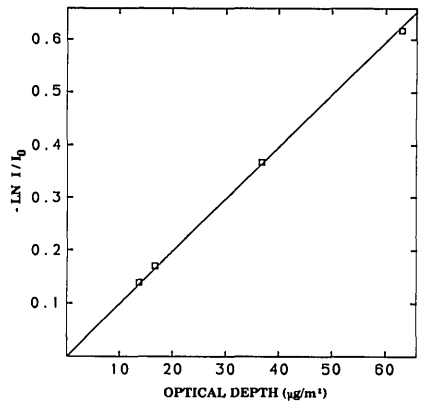

Fig. 4. Diagram of data used for cross-sectional determination.

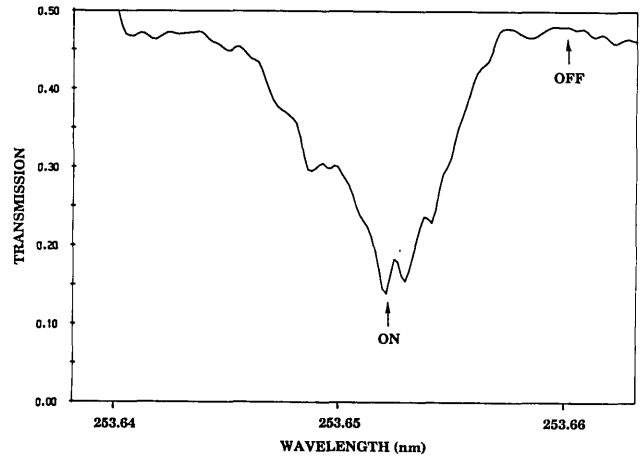

Fig. 5. Recording of the absorption line from mercury released from a 500-m distant chlorine–alkali plant. The transmission on the vertical scale has not been compensated for natural extinction and $1/R^2$ dependence.

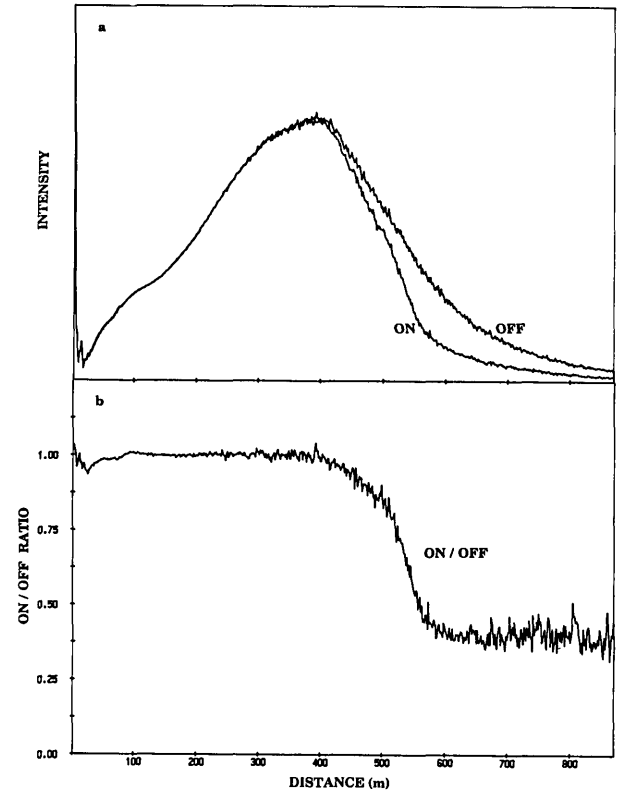

Fig. 6. (a) On/off-resonance lidar curves and (b) resulting DIAL curve.

could be performed directly on the outlet or downwind on the spreading plume with a free atmospheric path of ~900 m before the laser beam hit a hillside. The presence of Hg vapor in the clerestory outlet could be explicitly shown by measuring the decrease in the lidar signal over a 300-m path containing the plume while scanning the laser slowly over the Hg line. The absorption spectrum thus obtained is shown in Fig. 5. The on- and off-resonance wavelengths in the quantitative DIAL measurements are indicated in the figure.

Figure 6 shows an example from a DIAL measurement on the Hg plume. The curves in Fig. 6(a) show the detected signal intensity due to backscattered laser light for the on- and off-resonance wavelengths. The signal here is averaged over 1600 shots at each wavelength. The shape of the lidar curves is due to two factors: geometrical dependence and gain modulation of the photomultiplier. Figure 6(b) shows the resulting ratio of DIAL curve, where the significant effect of the plume is easily seen. By performing several se-

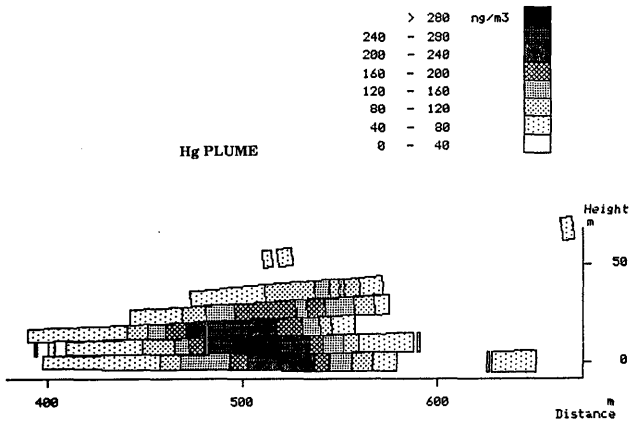

Fig. 7. Vertical scan of the Hg plume downwind from a chlorine–alkali plant.

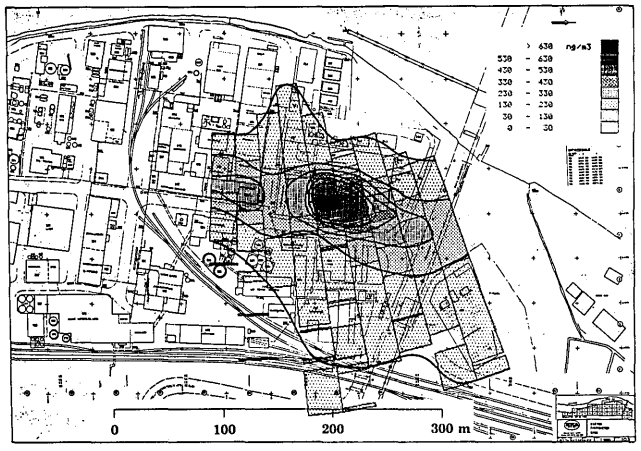

Fig. 8. Horizontal scan of Hg distribution over a chlorine–alkali plant.

quential measurements of this kind in different directions in a vertical section, the Hg concentration in the spreading plume could be charted. An example of this is shown in Fig. 7, where the Hg concentrations were evaluated from the DIAL curves with a range resolution of 45 m. The behavior of the fast-descending plume was studied in this way. The flux of Hg vapor through the vertical section was also measured by integrating the concentration over the area of the plume cross section and multiplying the integrated content by the wind velocity normal to the vertical section. In the example given here, the flux was found to be 30 g/h of atomic Hg vapor.

Another example of a Hg concentration map is shown in Fig. 8, where a horizontal scan at low height was performed. Several scans were averaged to give a more representative picture. The result here is copied directly onto a map of the plant. This is often a useful representation, e.g., to locate different sources. For clarity, isoconcentration lines are also drawn by hand beside the grey scale presented by the computer.

Some studies of the ability of the present system to measure the low background concentration of atomic mercury have also been performed. The typical range for concentration evaluation was found to be ~1 km with normal visibility. This limited range is due to the natural atmospheric extinction at these short wavelengths, which was measured to 1.2–1.6 km^{-1}, in good agreement with existing theory for Rayleigh scattering and empirical formulas for the Mie scattering contribution. The absorption by ozone gives a contribution of 0.3 km^{-1} for a typical background concentration of 10 ppb. A homogeneously distributed low concentration can be evaluated by fitting the DIAL curve with a straight line. The slope of this line then gives the average concentration over the path. Figure 9 shows an example of this kind. Several similar measurements were performed, also with the laser tuned off the Hg line, to estimate the noise in the concentration evaluation. The noise was found to be between 0.5 and 2 ng/m^3, depending on the atmospheric conditions. Unfortunately, during the period of the measurement only values close to or slightly over the noise

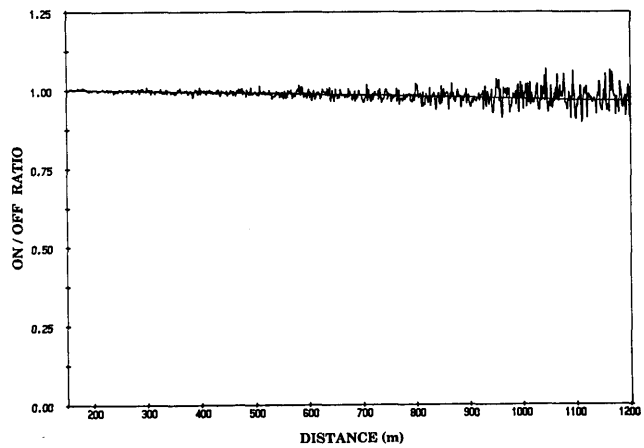

Fig. 9. Recording of Hg background concentration.

limit were detected. The small slope in Fig. 9 gives a concentration of 1.5 ± 1 ng/m^3.

IV. Hg Resonance Fluorescence

Lidar detection of atomic mercury is complicated by resonance fluorescence, as previously reported in Ref. 19. Because it occurs at the same wavelength as the detected backscattered light, resonance fluorescence cannot be separated spectrally from the signal. We have examined the effects of fluorescence on DIAL measurements both experimentally and theoretically, and present a technique for correcting for the effects of fluorescence.

For DIAL measurements, resonance fluorescence will usually only affect the on-resonance measurement. This can result in a signal for the on-resonance wavelength which is greater than that of the off-resonance wavelength. This effect is seen in the lidar curves shown in the lower part of Fig. 10(a). These were taken near the outlet of the clerestory at the chlorine–alkali plant and the sharp gradient in the mercury concentration results in a fluorescence peak at the on-resonance wavelength at the onset of absorption. The peak is also visible in the DIAL (upper)

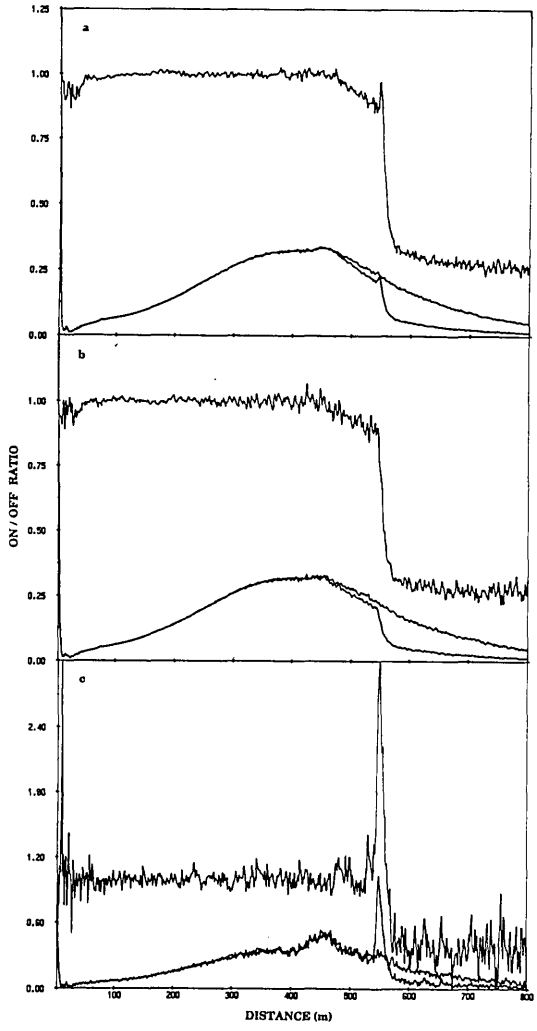

Fig. 10. Lidar/DIAL curves recorded for (a) both polarizations and (b) parallel and (c) perpendicular to the laser polarization.

curve which shows the ratio of the on- to off-resonance wavelengths. If evaluated over a suitably narrow interval, this would result in a seemingly negative mercury concentration. The qualitative effects of uncorrected resonance fluorescence are demonstrated in a model study described in the Appendix. These include a displacement of the calculated concentration curve to a position further from the lidar system, and a distortion of the signal. For small absorptions, the displacement is independent of the concentration present and depends solely on the ratio of the fluorescence backscattering coefficient to the nonresonant backscattering coefficient.

A simple argument demonstrates that the total concentration measured is not affected by resonance fluorescence. The natural fluorescence lifetime of the $6s6p^3P_1$ level in mercury is ~100 ns.[34] The quenching factor for Hg atoms in air is $\sim 2 \times 10^{-3}$, corresponding to a quenching time of 0.2 ns.[35] Thus, finite relaxation effects[36] are not significant, and the fluorescence signal is range resolved. The fluorescence from a given volume will be detected simultaneously with the backscattered signal, making the effective scattering at the resonance wavelength greater than that at the nonresonance (off) wavelength. Thus, errors in the DIAL signal due to fluorescence will be limited to the regions where mercury is present. Thus, the absorption of the returning signal from beyond a mercury plume is unaffected by fluorescence, and the total integrated concentration obtained is correct, even though the exact shape of the concentration calculated from the DIAL measurements may be incorrect.

To correct for the effects of resonance fluorescence, the strength of the fluorescence backscattering relative to the nonresonant Rayleigh and Mie backscattering must be known. While this ratio is treated as variable in the theory presented in the Appendix, it is difficult to determine this ratio for all points in a lidar curve. The ratio may vary due to particles in a plume or local variations in the quenching rate. Variation in the backscattering due to particles may be seen as increased scattering at the off-resonance signal above the level for clean air. Variation in the quenching rate is more difficult to determine. For the measurement at the chlorine–alkali plant, little scattering due to particles was observed, and the fluorescence-to-nonresonant backscattering ratio was treated as a constant. It is noted that the effects of fluorescence in this case of relatively clean air were small and that an increase in either backscattering or quenching would make the effects still smaller.

We have attempted to measure the fluorescence-to-nonresonant backscattering ratio through lidar measurements at orthogonal polarizations. An Ealing UV polarizer was inserted between the collecting telescope and the photomultiplier. The returning signal was found to be strongly polarized. Measurements were taken with the polarizer oriented to give maximum transmission and then at 90°. The resulting lidar curves are shown at the bottom of Figs. 10(b) and 10(c). All three data sets shown in Fig. 10 were taken during a span of 23 min. The relative scales for curves (b) and (c) differ by a factor of 10, so there is a difference in the backscattering signal of a factor of 15. This indicates that the scattering at this short wavelength is predominantly polarized. Rayleigh scattering, which preserves polarization, varies as $1/\lambda^4$. Mie scattering has a slower wavelength dependence and it maintains polarization if the scatterers are spherical. Nonspherical scatterers or multiple scattering may induce depolarization. The fluorescence signal, however, appears to be unpolarized. That is, the relative magnitudes of the two polarizations are about the same. This would indicate that the rate of elastic depolarizing collisions[37] is significantly greater than the quenching rate. Because the two curves were not recorded simultaneously, it is impossible to determine the exact ratio between the two polarizations. Because of the difference in polarization between the main backscattering signal and the fluorescence signal, a polarizer may be used to suppress the fluorescence effects. This could yield a factor of 2 reduction in the fluorescence effects for a completely polarized backscattered signal, and an unpolarized fluorescence signal. The factor F/B described in the Appendix was found to be 2×10^{-4} m^3/ng

from the height of the fluorescence peak shown in Fig. 10(c), the magnitudes of the background scattering in Figs. 10(b) and (c), and the calculated concentration from Fig. 10(a). With this value, the method described in the Appendix may be used to correct for the fluorescence. This was done for the curves shown in Fig. 10(a) and the results are shown as the solid curve in Fig. 11. The dashed curve is the result calculated without any correction for fluorescence. This curve is displaced from the position of the corrected curve by 10 m, in agreement with the expected displacement described in the Appendix. Additionally, the uncorrected curve is distorted, lying too low on the near side, and too high on the far side, as expected from the model study presented in the Appendix.

V. Conclusions

Lidar measurements of atomic mercury in the atmosphere have been demonstrated, yielding 3-D maps of the gas distribution. High laser pulse energies and a narrow laser linewidth were found to be essential for this development. We found that the effects of fluorescence led to a displacement of the calculated concentration curve and a distortion of the concentration profile. We have presented a theoretical technique for correcting these effects, and an experimental technique for measuring the fluorescence to background factor necessary to implement this correction. The Hg lidar technique shows high potential for pollution monitoring and also for studies of geophysical phenomena. A search for mercury in the atmosphere at Icelandic geothermal fields has already been performed[38] and further studies of atmospheric mercury of geophysical origin seem to be of considerable interest.

The authors are grateful to B. Galle for helping with the practical arrangements for the field work. This work was supported by the Swedish Board for Space Activities, The Swedish Environmental Protection Board, and the Swedish Natural Science Research Council. One of us (G.W.F.) would like to thank the U.S. National Science Foundation for a grant enabling him to spend a year at the Lund Institute of Technology.

Appendix: Correction for Resonance Fluorescence

The lidar equation for the detected power $P(\lambda,R)$ at a wavelength λ, resulting from atmospheric backscattering at a distance R, may be written as

$$P_{AS}(\lambda,R) = C(\lambda,R)\beta(\lambda,R)\exp\left\{-2\int_0^R [N_i(R')\sigma_i(\lambda) + N_r(R')\sigma_r(\lambda)]dR'\right\}. \quad \text{(A1)}$$

$C(\lambda,R)$ is a factor which includes such effects as the emitted laser energy and temporal profile, the laser's effective beam area at range R, the overlap of the transmitted beam and the receiving optics field of view, the solid angle of the backscattered flux captured by the receiving optics, and the optical efficiency of the collection optics, filters, and the detector. $\beta(\lambda,R)$ is the volume atmospheric backscattering coefficient. $N_i(R)$ and $\sigma_i(\lambda)$, and $N_r(R)$ and $\sigma_r(\lambda)$ are the concentrations and absorption cross sections of an atmospheric constituent of interest and the remaining constituents, respectively. A similar equation may be written for the detected power due to resonance fluorescence, $P_F(\lambda,R)$, for the constituent of interest:

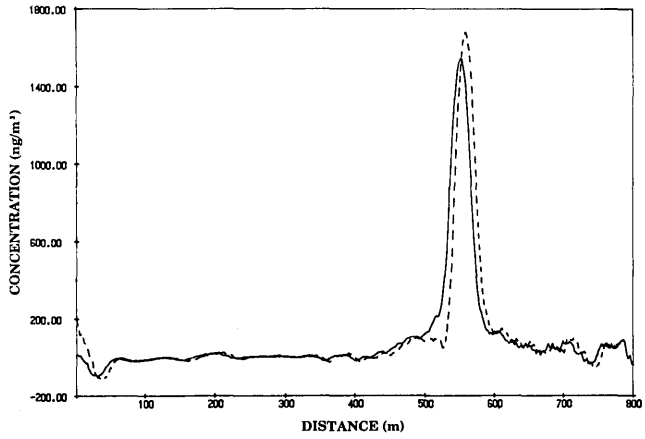

Fig. 11. Mercury concentration curves calculated with (solid line) and without (dashed line) correction for fluorescence.

$$P_F(\lambda,R) = C(\lambda,R)N_i(R)F(\lambda,R)\exp\left\{-2\int_0^R [N_i(R')\sigma_i(\lambda) + N_r(R')\sigma_r(\lambda)]dR'\right\}, \quad \text{(A2)}$$

where $F(\lambda,R)$ represents the normalized fluorescence scattering coefficient, which includes the effects of the absorption cross section, the quantum efficiency for resonance fluorescence, and quenching. It is assumed here, as discussed in Sec. IV, that the lifetime of the upper level is much shorter than the laser pulse length. These two equations may be combined to yield the total detected power due to atmospheric and fluorescence scattering:

$$P(\lambda,R) = C(\lambda,R)[\beta(\lambda,R) + N_i(R)F(\lambda,R)] \times \exp\left\{-2\int_0^R [N_i(R')\sigma_i(\lambda) + N_r(R')\sigma_r(\lambda)]dR'\right\}. \quad \text{(A3)}$$

DIAL measurements are taken at two closely spaced wavelengths, that on resonance λ_{on}, and that off resonance λ_{off}. It is then assumed that the factors $\beta(\lambda,R)$ and $\sigma_r(\lambda)$ are the same for the two wavelengths, while $C(\lambda_{on},R)$ and $C(\lambda_{off},R)$ are related by a constant. The ratio of the powers for the on- and off-resonance wavelengths, $\hat{P}(R) = P(\lambda_{on},R)/P(\lambda_{off},R)$, may be written as

$$\hat{P}(R) = \left[1 + \frac{N_i(R)F(R)}{\beta(R)}\right]\exp\left[-2\sigma_{diff}\int_0^R N_i(R')dR'\right], \quad \text{(A4)}$$

where $\sigma_{diff} = \sigma(\lambda_{on}) - \sigma(\lambda_{off})$ represents the difference between the cross sections for the on- and off-resonance wavelengths, the fluorescence backscattering for the off-resonance wavelength is assumed to be negligible compared to the atmospheric backscattering, and the power ratio has been normalized by the factor $C(\lambda_{on},R)/C(\lambda_{off},R)$. $F(R)$ and $\beta(R)$ are understood to

apply to the wavelength λ_{on} and N now refers to the concentration of the constituent of interest. This equation may be written in an (exact) differential form:

$$\hat{P}(R+\Delta R)=\frac{\hat{P}(R)}{1+\frac{F(R)}{\beta(R)}N(R)}\left[1+\frac{F(R+\Delta R)}{\beta(R+\Delta R)}N(R+\Delta R)\right]$$

$$\times\exp\left[-2\sigma_{\text{diff}}\int_{R}^{R+\Delta R}N(R')dR'\right]. \tag{A5}$$

Equation (A5) may alternatively be written as

$$\hat{P}(R+\Delta R)=\hat{P}_{NF}(R)\left[1+\frac{F(R+\Delta R)}{\beta(R+\Delta R)}N(R+\Delta R)\right]$$

$$\times\exp\left[-2\sigma_{\text{diff}}\int_{R}^{R+\Delta R}N(R')dR'\right], \tag{A6}$$

where $\hat{P}_{NF}(R)$ represents the on- to off-resonance power ratio that would be present if there were no fluorescence. This equation shows explicitly that, for negligible upper level relaxation times, the power ratio returning from a point $R+\Delta R$ is not dependent on the fluorescence contributions from other points. If the absorption over the length ΔR is small, this equation may be rewritten as

$$\hat{P}(R+\Delta R)\approx\hat{P}_{NF}(R)\left[1+\frac{F(R+\Delta R)}{\beta(R+\Delta R)}N(R+\Delta R)-2\sigma_{\text{diff}}\bar{N}\Delta R\right], \tag{A7}$$

where $\bar{N}$ represents a value averaged between R and $R+\Delta R$. For small ΔR such that N, F, and β are about constant, then

$$\hat{P}(R+\Delta R)\approx\hat{P}_{NF}(R)\left[1+\bar{N}\left(\frac{F}{\beta}-2\sigma_{\text{diff}}\Delta R\right)\right]. \tag{A8}$$

Note that, for a displacement ΔR given by

$$\Delta R\approx\frac{F}{2\sigma_{\text{diff}}\beta}, \tag{A9}$$

the displaced fluorescence power ratio, $\hat{P}(R+\Delta R)$, is equal to the undisplaced power ratio in the absence of fluorescence. As this relation holds for every point R (so long as the concentration does not vary greatly over the width ΔR), the dominant effect of fluorescence is seen as a displacement of the DIAL signal away from the observer by a distance of $\sim F/2\sigma\beta$. Note that this displacement is independent of the concentration N. Thus, to first order, an equally large displacement will be found for small concentrations as for large concentrations. For the mercury differential cross section given in Sec. III, 9.8×10^{-6} m^2/ng, and the ratio F/β given in Sec. IV, 2×10^{-4} m^3/ng, the displacement is ~10 m. Simulation studies of fluorescence lidar[39] have found a similar type of shift, but in that case, absorption causes the measured fluorescence curve to be shifted toward the observer.

This displacement and other effects of resonance fluorescence may be illustrated with a simulation. Figure 12(a) shows the $\hat{P}$ ratio, or DIAL curves for a simulated rectangular mercury cloud, of width 75 m and a uniform concentration of 1000 ng/m^3. The solid line shows the DIAL curve if there were no fluorescence and the dashed line shows the DIAL curve when the normalized fluorescence ratio, F/β, is constant, equal to 2×10^{-4} m^3/ng. While a Gaussian or other smoothly varying cloud is more typical of real clouds, a rectangular cloud was chosen to better demonstrate the effects of resonance fluorescence and a method to correct for these effects. The displacement between the two curves agrees with the expression in Eq. (A9), but at the sharp concentration gradients at the edges, other effects appear. There the mercury concentration changes considerably in the displacement distance given by Eq. (A9), and discontinuities are present at the boundaries of the cloud.

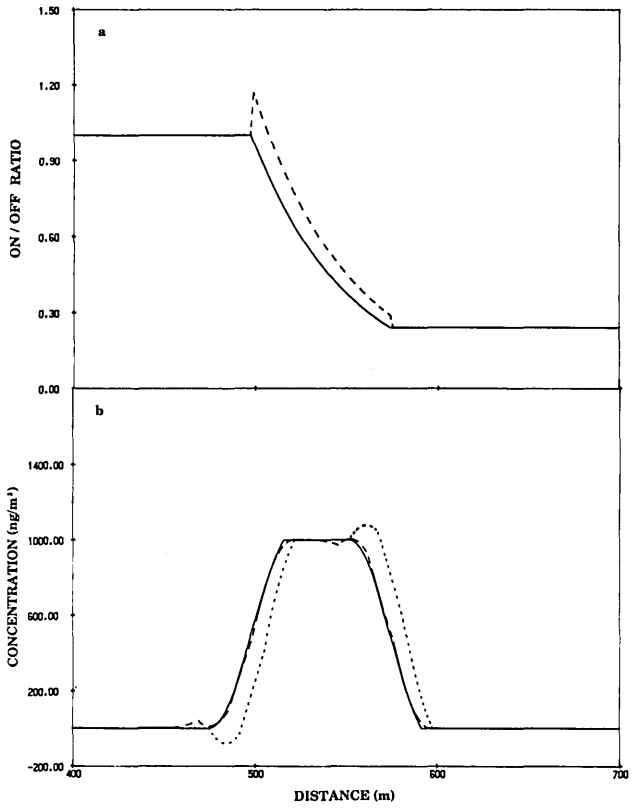

Fig. 12. DIAL curves for a simulated Hg cloud: (a) displaying the fluorescence effect (dashed line) and (b) calculated concentration profiles obtained with (dashed line) and without (dotted line) correction for fluorescence.

The effects of fluorescence may be corrected using Eq. (A5). This is similar in form to the differential equation normally used to evaluate concentrations from a DIAL curve based on absorption alone. However, an additional fluorescence term contains the concentration to be evaluated, $N(R+\Delta R)$, and the absorption and fluorescence terms effectively have opposite signs [see Eq. (A7), for example]. This makes the concentration calculation more sensitive to noise than for absorption alone, and, in the worst case, for an evaluation interval ΔR given by Eq. (A9) there is no dependence on the concentration at all. However, when integrating in the opposite direction, that is, from larger R to smaller R, both the absorption and

fluorescence terms have the same sign, and the integration is less sensitive to noise. This is the approach that has been used to solve for the fluorescence-corrected concentration.

Using subscript 1 to denote the position R and 2 to denote $R + \Delta R$, and substituting the average concentration value $(N_1 + N_2)/2$ in the exponential, Eq. (A5) may be written as

$$\hat{P}_2 = \frac{\hat{P}_1}{1 + \frac{F_1}{\beta_1} N_1} \left[1 + \frac{F_2}{\beta_2} N_2 \right] \exp[-\sigma_{\text{diff}}(N_1 + N_2)\Delta R]. \quad \text{(A10)}$$

This can be rewritten as a transcendental equation for the quantity N_1 in terms of N_2 and the known power ratios at points 1 and 2, $\hat{P}_1$ and $\hat{P}_2$:

$$\left[1 + \frac{F_1}{\beta_1} N_1 \right] \exp(\sigma_{\text{diff}} N_1 \Delta R) = \frac{\hat{P}_1}{\hat{P}_2} \left[1 + \frac{F_2}{\beta_2} N_2 \right] \exp(-\sigma_{\text{diff}} N_2 \Delta R). \quad \text{(A11)}$$

This equation may be solved using Newton's method[40] for all values of N_1 and converges typically in one to three iterations. In evaluating an experimentally measured lidar curve, noise in the data combined with a limited number of samples necessitates spatial averaging. This was done with a sliding average technique as is done in the evaluation of lidar curves without fluorescence. Because of the large separation between points 1 and 2 for a sliding average technique, the solution of Eq. (A11) is sensitive to overshoot and undershoot. This is partly due to the dependence of the solution for the concentration N_1 on previously determined concentrations N_2. This is not a problem in the solution of absorption alone. In evaluating Eq. (A11) for longer integration ranges ΔR, it was found that keeping the resulting value of N_1 and storing it at position 1 (appropriate for fluorescence alone, this is somewhat like a forward difference approximation[41]), results in underdamped overshoot when there is a large concentration gradient and absorption is predominant. When the calculated value is stored as a value of $\bar{N}$, or $(N_1 + N_2)/2$, at a position midway between 1 and 2 (appropriate for absorption alone, this is similar to a central difference solution[41]), undershoot occurs for large concentration gradients when fluorescence is predominant. Very good results were found when each evaluation was stored as the interpreted value between N_1 and N_2 at a distance

$$\frac{\Delta R}{2} \left[\frac{\sigma_{\text{diff}} \Delta R}{\frac{F}{\beta} + \sigma_{\text{diff}} \Delta R} \right] \quad \text{(A12)}$$

toward point 2 from point 1. Thus, when fluorescence effects are dominant (large F/β), the evaluation is more like a forward difference approximation, but when absorption is dominant (small F/β), it becomes more like a central difference solution.

The performance of this technique was evaluated using the DIAL curves in Fig. 12(a), a demanding test case because of the infinitesimally sharp concentration gradients. The resulting concentration curves are shown in Fig. 12(b). The curves were calculated using a sliding average technique with a path length of 30 m and an average length of 11 points (15 m). These lengths are typical for an experimental curve with good signal-to-noise ratio. Shown as the solid line in Fig. 12(b) is the concentration curve evaluated from the solid line in Fig. 12(a), that without fluorescence. The dotted line in Fig. 12(b) shows the concentration calculated from the DIAL curve containing fluorescence [the dashed line in Fig. 12(a)] evaluated in the normal manner. This curve is shifted by the expected displacement, and there is additionally a dip on the near side of the concentration cloud and an overshoot on the far side. The dashed line in the figure shows the concentration calculated from the same DIAL curve but evaluated using Eq. (A11) together with Eq. (A12). This curve follows closely the proper, solid line, with some small transients at the corners.

References

1. J. O. Nriagu, Ed., *The Biogeochemistry of Mercury in the Environment* (Elsevier/North-Holland, Amsterdam, 1979).
2. O. Lindqvist and H. Rodhe, "Atmospheric Mercury—a Review," Tellus **37B**, 136 (1985).
3. Q. Bristow and I. R. Jonasson, "Vapour Sensing for Mineral Exploration," Can. Min. J. **93**, 39 (1972).
4. J. H. McCarthy, Jr., "Mercury Vapor and Other Volatile Components in the Air as Guides to Ore Deposits," J. Geochem. Explor. **1**, 143 (1972).
5. E. Kromer, G. Friedrich and P. Wallner, "Mercury and Mercury Compounds in Surface Air, Soil Gas, Soils and Rocks," J. Geochem. Explor. **15**, 51 (1980).
6. R. W. Klusman and J. D. Webster, "Meteorological Noise in Crustal Gas Emission and Relevance to Geochemical Exploration," J. Geochem. Explor. **15**, 63 (1981).
7. J. C. Varekamp and P. R. Buceck, "Hg Anomalies in Soils: a Geochemical Exploration Method for Geothermal Areas," Geothermics **12**, 29 (1983).
8. D. E. Robertson, E. A. Crecelius, J. S. Fruchter, and J. D. Ludwick, "Mercury Emissions from Geothermal Power Plants," Science **196**, 1094 (1977).
9. V. Z. Furzov, N. B. Volfson, and A. G. Khvalovskiy, "Results of a Study of Mercury Vapour in the Tashkent Earthquake Zone," Dokl. Acad. Nauk SSSR **179**, 208 (1968).
10. J. C. Varekamp and P. R. Buseck, "Mercury Emissions from Mount St. Helens During September 1980," Nature London **293**, 555 (1981).
11. F. Slemr, W. Seiler, and G. Schuster, "Latitudinal Distribution of Mercury over the Atlantic Ocean," J. Geophys. Res. **86**, 1159 (1981).
12. S. H. Williston, "Mercury in the Atmosphere," J. Geophys. Res. **73**, 7051 (1968).
13. C. Brosset, "Total Airborne Mercury and Its Possible Origin," Water Air Soil Pollut. **17**, 37 (1982).
14. W. F. Fitzgerald and G. A. Gill, "Subnanogram Determination of Mercury by Two-Stage Gold Amalgamation and Gas Phase Detection Applied to Atmospheric Analysis," Anal. Chem. **51**, 1714 (1979).
15. F. Slemr, W. Seiler, C. Eberling, and P. Roggendorf, "The Determination of Total Gaseous Mercury in Air at Background Levels," Anal. Chim. Acta **110**, 35 (1979).
16. J. C. Robbins, "Zeeman Spectrometer for Measurements of Atmospheric Mercury Vapour," in *Geochemical Exploration*, M. J. Jones, Ed. (Institute of Mining & Metallurgy, London, 1973), p. 315.

17. D. K. Killinger and A. Mooradian, Eds., *Optical and Laser Remote Sensing* (Springer-Verlag, Berlin, 1983).
18. R. M. Measures, *Laser Remote Sensing* (Wiley-Interscience, New York, 1984).
19. M. Aldén, H. Edner, and S. Svanberg, "Remote Measurement of Atmospheric Mercury Using Differential Absorption Lidar," Opt. Lett. **7,** 221 (1982).
20. H. Edner, S. Svanberg, L. Unéus, and W. Wendt, "Gas-Correlation Lidar," Opt. Lett. **9,** 493 (1984).
21. H. Edner, A. Sunesson, S. Svanberg, L. Unéus, and S. Wallin, "Differential Optical Absorption Spectroscopy System Used for Atmospheric Mercury Monitoring," Appl. Opt. **25,** 403 (1986).
22. U. Platt, D. Perner, and H. W. Pätz, "Simultaneous Measurement of Atmospheric CH_2O, O_3, and NO_2 by Differential Optical Absorption," J. Geophys. Res. **84,** 6329 (1979).
23. U. Platt and D. Perner, "Measurements of Atmospheric Trace Gases by Long-Path Differential UV/Visible Absorption Spectroscopy," in Ref. 17.
24. H. Edner, K. Fredriksson, A. Sunesson, S. Svanberg, L. Unéus, and W. Wendt, "Mobile Remote Sensing System for Atmospheric Monitoring," Appl. Opt. **26,** 4330 (1987).
25. C. Granier, J. P. Jégou, and G. Megie, "Resonant Lidar Detection of Ca and Ca^+ in the Upper Atmosphere," Geophys. Res. Lett. **12,** 10 (1985).
26. K. H. Fricke and U. von Zahn, "Mesopause Temperatures Derived from Probing the Hyperfine Structure of the D_2 Resonance Line of Sodium by Lidar," J. Atmos. Terr. Phys. **47,** 499 (1985).
27. A. Sunesson, "Construction of a Multipass Absorption Cell," Lund Reports on Atomic Physics LRAP-46, Lund Institute of Technology (1986).
28. Y. Nishimura and T. Fujimoto, "λ = 2537 Å Line from a Low-Pressure Mercury Discharge Lamp. Emission Profile and Line Absorption by a Gas Containing a Mercury Vapor," Appl. Phys. B **38,** 91 (1985).
29. G. Herzberg, "Forbidden Transitions in Diatomic Molecules. II. The $^3\Sigma_u^+$–$^3\Sigma_g^-$ Absorption Bands of the Oxygen Molecule," Can. J. Phys. **30,** 185 (1952).
30. G. Herzberg, "Forbidden Transitions in Diatomic Molecules. III. New $^1\Sigma_u^-$–$^3\Sigma_g^-$ and $^3\Delta_u$–$^3\Sigma_g^-$ Absorption Bands of the Oxygen Molecule," Can. J. Phys. **31,** 657 (1953).
31. D. A. Ramsay, "High-Resolution Studies of the Near-Ultraviolet Bands of Oxygen: I: The $c^1\Sigma_u^-$–$X^3\Sigma_g^-$ System," Can. J. Phys. **64,** 717 (1986).
32. P. M. Borrell, P. Borrell, and D. A. Ramsay, "High-Resolution Studies of the Near-Ultraviolet Bands of Oxygen: II: The $A^3\Sigma_u^+$–$X^3\Sigma_g^-$ System," Can. J. Phys. **64,** 721 (1986).
33. B. Coquart and D. A. Ramsay, "High-Resolution Studies of the Near-Ultraviolet Bands of Oxygen: III: The $A'^3\Delta_u$–$X^3\Sigma_g^-$ System," Can. J. Phys. **64,** 726 (1986).
34. J. Brossel and F. Bitter, "A New "Double Resonance" Method for Investigating Atomic Energy Levels," Phys. Rev. **86,** 308 (1952).
35. H. Inaba, "Detection of Atoms and Molecules by Raman Scattering and Resonance Fluorescence," in *Laser Monitoring of the Atmosphere*, E. D. Hinkley, Ed. (Springer-Verlag, Berlin, 1976), p. 182.
36. H. Kildal and R. L. Dyer, "Comparison of Laser Methods for the Remote Detection of Atmospheric Pollutants," Proc. IEEE **59,** 1644 (1971).
37. P. M. Doherty and D. R. Crosley, "Polarization of Laser-Induced Fluorescence in OH in an Atmospheric Pressure Flame," Appl. Opt. **23,** 713 (1984).
38. H. Edner, G. Faris, A. Sunesson, S. Svanberg, J. Ö. Bjarnasson, H. Kristmannsdottir, and K. H. Sigurdsson, "Lidar Search for Atmospheric Atomic Mercury in Icelandic Geothermal Fields," manuscript in preparation for J. Geophys. Res.
39. R. M. Measures and G. Pilon, "A Study of Tunable Laser Techniques for Remote Mapping of Specific Gaseous Constituents of the Atmosphere," Opto-Electronics **4,** 141 (1972).
40. F. S. Acton, *Numerical Methods that Work* (Harper & Row, New York, 1970), p. 51.
41. G. P. Smith, *Numerical Solution of Partial Differential Equations: Finite Difference Methods* (Clarendon, Oxford, 1985), p. 7.

Mercury Ion Laser-Cooled To Limit

Scientists at NIST's Time and Frequency Division, Boulder, Colo., have succeeded for the first time in laser-cooling a bound atomic ion to its fundamental limit. "We pushed the atom into the ground state of its confining well. That's the end of cooling for a bound particle," says project leader David J. Wineland. Their finding is important for spectroscopy, a study of the nature of matter through various radiations it emits. **One result may be the development of a highly sensitive spectrum analyzer.** A report on their work appears in the Jan. 23, 1989, issue of ***Physical Review Letters.*** They shined laser light on a mercury ion sideband frequency generated by the Doppler effect associated with thermal motion. The result was to reduce the ion's kinetic energy, limit its movement, and sharpen its spectral features. The ion was confined in a radio frequency "trap."